Detection of Nonlinear Behavior Induced by Hard Limiting in Voltage Source Converters in Wind Farms Based on Higher-order Spectral Analysis

Zetian Zheng, Shaowei Huang, Qiangsheng Bu, Chen Shen, and Jun Yan

***Abstract*—In recent years, sub-synchronous oscillation accidents caused by wind power integration have received extensive attention. The recorded constant-amplitude waveforms can be induced by either linear or nonlinear oscillation mechanisms. Hence, the nonlinear behavior needs to be distinguished prior to choosing the analysis method. Since the 1960s, the higher-order statistics (HOS) theory has become a powerful tool for the detection of nonlinear behavior (DNB) in production quality control wherein it has mainly been applied to mechanical condition monitoring and fault diagnosis. This study focuses on the hard limiters of the voltage source converter (VSC) control systems in the wind farms and attempts to detect the nonlinear behavior caused by bi- or uni-lateral saturation hard limiting using the HOS analysis. First, the conventional describing function is extended to obtain the detailed frequency domain information on the bi- and uni-lateral saturation hard limiting. Furthermore, the bi- and tri-spectra are introduced as the HOS, which are extended into bi- and tri-coherence spectra to eliminate the effects of the linear parts on the harmonic characteristics of hard limiting in the VSC control system, respectively. The effectiveness of the HOS in the DNB and the classification of the hard-limiting types is proven, and its detailed derivation and estimation procedure is presented. Finally, the quadratic and cubic phase coupling in the signals is illustrated, and the performance of the proposed method is evaluated and discussed.**

***Index Terms*—Bi-coherence spectrum, detection of nonlinear behavior, hard limiting, higher-order statistics, tri-coherence spectrum, voltage source converter, wind farms.**

I. Introduction

With the implementation of the energy development strategy in China, the installation capacity of wind power has increased [1]. However, the stability problems caused by wind power integration are more serious, with sub-synchronous oscillation (SSO) being the most severe [2]. After SSO accidents, the amplitudes of the recorded accident waveforms tend to be constant because the transition process is very fast. Many studies have analyzed SSO based on the weak-damping assumption. Here, the researchers linearized the power-system dynamic equations and conducted studies using linear analysis methods, including the eigenvalue [3], dynamic equivalent [4], [5], impedance [6], [7], and complex torque coefficient [8], [9] methods. However, nonlinear effects such as hard limiting in the control system of the wind generators, while the induced self-sustained oscillation also exhibits a constant amplitude.

Current research on nonlinear oscillation analysis can be broadly classified into two categories.

1) Under small perturbations, constant-amplitude oscillations induced by the negative damping of the voltage source converter (VSC) generally begin with divergent oscillations near the equilibrium point of the system. Owing to the influence of the nonlinear factors in the VSC, such as hard limiting and pulse-width modulation (PWM) saturation, the oscillations will not continue to diverge, thereby resulting in constant-amplitude self-sustained oscillations [10]. To address the constant-amplitude oscillations caused by hard limiting, the describing function (DF) can be used to model the nonlinear parts of the system, combined with a small-signal model of the system to analyze the characteristics of the oscillations. For example, [11] established an impedance model of a VSC considering the PWM saturation and analyzed the mechanism of the constant-amplitude oscillations. References [12] and [13] considered the bi-lateral hard limiting of the current and DC-voltage loops of a grid-connected VSC, respectively, and used the Nyquist criterion to obtain the approximate calculation formula for the oscillation frequency and amplitude.

2) Under large disturbances such as faults, self-sustained oscillations can be caused by the effects of nonlinear parts such as hard limiting. Meanwhile, if the corresponding hard-limiting parts are removed, the system can return to its original equilibrium point after the large disturbance. Current research on the mechanism of oscillations under large disturbances is still in the preliminary stage. Reference [14] studied the self-sustained oscillations caused by the hard limiting of static var generators (SVGs) in double-fed induction generators after a fault and analyzed the influence of the system parameters on the non-smooth bifurcations. Reference [15]

Manuscript received: November 29, 2022; revised: March 2, 2023; accepted: June 9, 2023. Date of CrossCheck: June 9, 2023. Date of online publication: August 16, 2023.

This work was supported by the State Grid Guide Project (No. 5108-202218030A-1-1-ZN).

Z. Zheng, S. Huang, C. Shen (corresponding author), and J. Yan are with the State Key Laboratory of Power Systems, Department of Electrical Engineering, Tsinghua University, Beijing 100084, China (e-mail: zzt_thu@qq.com; huangsw@tsinghua.edu.cn; shenchen@mail.tsinghua.edu.cn; 458783027@qq.com).

Q. Bu is with State Grid Jiangsu Electric Power Co., Ltd. Research Institute, Nanjing, China (e-mail: tc16002315@163.com).

DOI: 10.35833/MPCE.2022.000784

analyzed the instable oscillations of the grid-connected VSCs at the positive-damping equilibrium points after they experienced large disturbances. When the *d*-axis current reaches its hard limit, the outer control loop of the DC voltage loses its effectiveness, thereby resulting in electromagnetic oscillations in the system, accompanied by a continuous increase in the DC voltage.

The mechanism and corresponding analysis method of the nonlinear oscillations are different from those of linear oscillations. The direct analysis of the amplitude and frequency of the SSO using a linearized method and adoption of the corresponding measures to suppress the oscillation are unacceptable. Hence, before choosing the analysis method, it is important to determine the type of oscillation (linear or nonlinear) from the waveform records.

Since its emergence in the early 1960s, the higher-order statistics (HOS) theory has become a powerful tool for the condition monitoring and fault diagnosis of the mechanical equipment. Its applications include harmonic retrieval [16], system identification [17], and feature extraction [18]. Furthermore, it is used for the detection of nonlinear behavior (DNB) [19]. Based on the bi-spectrum, the definitions of the bi-coherence spectrum and inverted bi-spectrum are presented in [20] and [21], respectively, and different statistical indicators based on HOS for DNB have been introduced.

Inspired by the aforementioned ideas in 1995, the researchers of power systems applied the bi-spectral analysis to the fault diagnosis and condition monitoring of the three-phase induction motors to analyze and identify motor asymmetric faults and stator winding failure [22]. Subsequently, studies on the fault diagnosis using HOS have achieved considerable results. Reference [23] detected and identified asymmetric faults in induction motors by measuring the vibration data and analyzing the motor nonlinearity using the bi-coherence spectrum. In [24], considering the Gaussian and non-Gaussian noises in the mechanical signals, a new rolling bearing detection method was proposed, which integrated the bi-spectral analysis with the improved ensemble empirical mode decomposition.

In wind farms, [25] used a modulated signal bi-spectrum detector to diagnose bearing faults in doubly-fed induction generators. Reference [26] used a bi-spectral analysis to identify single-point defects in rolling bearings. Reference [27] proposed an improved signal separation method based on the Vold-Kalman filter and HOS analysis for rotating mechanical systems under strong background noise.

However, the current applications of the bi-spectral analysis focus on the mechanical defects in the power systems, and few studies have analyzed the nonlinearity of the control modules in these systems, particularly in wind farms.

In this study, we focus on the hard limiters in the VSC, which is a crucial component of wind turbines and SVGs. To apply the HOS to the hard-limiting DNB in the control system of VSCs in wind farms, four aspects must be considered: ① suitability of the HOS for characterizing the nonlinearity of the hard limiters in the VSC control system and selection of an appropriate HOS; ② approach to determine the characteristics using only the waveforms collected at the terminal of the VSC; ③ method to detect the nonlinear behavior caused by the bi- or uni-lateral saturation hard limiting, which is considered as the source of the nonlinearity in this study; and ④ approach to improve the effectiveness and quality of the spectrum.

By fully addressing the aforementioned aspects, this study seeks to analytically prove the effectiveness of the HOS applied to the DNB induced by hard limiting in the VSC control system.

The rest of this paper is organized as follows. Section II extends the conventional DF and analyzes the two types of hard limiting. In Section III, the HOS is introduced. In Section IV, the VSC control system is modeled while the HOS-based hard-limiting DNB is analyzed and confirmed. The detailed procedures for the hard-limiting DNB in the VSC control system are described in Section V. Its effectiveness is demonstrated through case studies in Section VI. Finally, Section VII draws the conclusions.

II. Analysis of Harmonic Characteristics of Hard Limiting

The DF [28] has been effectively used to analyze the characteristics of the self-sustained oscillations or limit cycles caused by nonlinearity. In the conventional DF, only the first-order Fourier series of the oscillation are maintained. In the DNB, however, the higher-order terms are required to distinguish the self-sustained oscillations induced by hard limiting from the negatively damped oscillations induced by incorrectly configured control parameters. Hence, the DF method is introduced and extended, and the harmonic characteristics of the bi- and uni-lateral saturation hard limiting are discussed.

A. Extended DF

As shown in Fig. 1, the input signal of the studied nonlinear part $x(t)$ is assumed to be sinusoidal as expressed below:

$$x(t) = A\sin\omega t \tag{1}$$

where A and ω are the amplitude and frequency of the sinusoidal input signal, respectively.

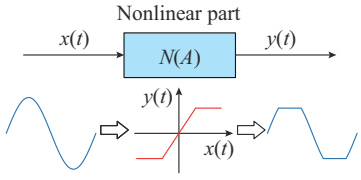

Fig. 1. Typical hard limiter with a sinusoidal input.

The hard-limit output $y(t)$ is a periodic nonsinusoidal signal, which can be expanded into a Fourier series as expressed below:

$$y(t) = A_0 + \sum_{n=1}^{\infty}\left(A_n\cos n\omega t + B_n\sin n\omega t\right) \tag{2}$$

where A_0 is the magnitude of the DC component; and A_n and B_n are the coefficients of the cosine and sine parts of

the n^{th} Fourier harmonic, respectively.

In the conventional DF-based analysis method, the nonlinear part is considered oddly symmetrical and the linear part is considered low-pass. Consequently, $A_0=0$, and $y(t)$ can be approximated as:

$$y(t)\approx y_1(t)=A_1\cos\omega t+B_1\sin\omega t=Y_1\mathrm{e}^{\mathrm{j}\varphi_1 t} \tag{3}$$

where $Y_1=\sqrt{A_1^2+B_1^2}$ and $\varphi_1=\arctan\dfrac{B_1}{A_1}$, and we have

$$\begin{cases} A_1=\dfrac{1}{\pi}\displaystyle\int_0^{2\pi}y(t)\cos\omega t\mathrm{d}(\omega t) \\ B_1=\dfrac{1}{\pi}\displaystyle\int_0^{2\pi}y(t)\sin\omega t\mathrm{d}(\omega t) \end{cases} \tag{4}$$

The ratio of the first-order Fourier series of $y(t)$ to the magnitude of the input signal is defined as the DF of the nonlinear part, i.e., $N(A)$.

$$N(A)=\frac{Y_1}{A}\mathrm{e}^{\mathrm{j}\varphi_1} \tag{5}$$

To extend the DF method, the higher-order harmonic coefficients A_n and B_n in (2) are calculated as:

$$\begin{cases} A_n=\dfrac{1}{\pi}\displaystyle\int_0^{2\pi}x(t)\cos n\omega t\mathrm{d}(\omega t) \\ B_n=\dfrac{1}{\pi}\displaystyle\int_0^{2\pi}x(t)\sin n\omega t\mathrm{d}(\omega t) \end{cases} \tag{6}$$

B. Bi-lateral Saturation Hard Limiting

As shown in Fig. 2(a), when a sine wave $x(t)=A\sin\omega t$ passes through a time-domain bi-lateral saturation hard limiter, its upper and lower parts that exceed the limits are set at the limit values, as expressed below:

$$y(t)=\begin{cases} -a & x(t)<-a \\ x(t) & -a\le x(t)\le a \\ a & x(t)>a \end{cases} \tag{7}$$

where a $(a>0)$ is the upper hard limit.

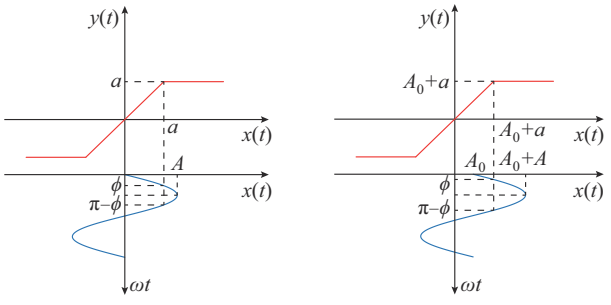

Fig. 2. Time-domain characteristics of bi- and uni-lateral saturation hard limiting. (a) Bi-lateral saturation. (b) Uni-lateral saturation.

Here, the bi-lateral saturation hard limiting is oddly symmetrical, and the output periodic signal is an odd function. Hence, the coefficients of the DC and cosine components in the Fourier series are 0, that is, $A_n=0$ $(n=0,1,2,\ldots)$. According to (4), the fundamental Fourier coefficient of the output signal can be obtained as:

$$\begin{aligned} B_1&=\frac{1}{\pi}\int_0^{2\pi}x(t)\sin\omega t\mathrm{d}(\omega t)=\frac{2}{\pi}\left(\int_0^{\phi}A\sin^2\omega t\mathrm{d}(\omega t)+\right. \\ &\left.\int_{\phi}^{\pi-\phi}a\sin\omega t\mathrm{d}(\omega t)+\int_{\pi-\phi}^{\pi}A\sin^2\omega t\mathrm{d}(\omega t)\right)= \\ &\frac{2A}{\pi}\left(\arcsin\frac{a}{A}+\frac{a}{A}\sqrt{1-\left(\frac{a}{A}\right)^2}\right) \end{aligned} \tag{8}$$

The n^{th} Fourier coefficient is calculated similarly, and the results show that

$$B_{2n}=0\quad n=1,2,3,\ldots \tag{9}$$

The detailed calculation results are presented in Appendix A Table AI.

C. Uni-lateral Saturation Hard Limiting

As shown in Fig. 2(b), when a sine wave $x(t)=A\sin\omega t$ passes through a time-domain uni-lateral saturation hard limiter, the upper or lower (depending on the actual situation) part that exceeds the limit is set at the limit value. Without loss of generality, the corresponding equations of the upper hard limit are expressed as:

$$y(t)=\begin{cases} x(t) & x(t)\le A_0+a \\ A_0+a & x(t)>A_0+a \end{cases} \tag{10}$$

where A_0 is the offset of the sinusoidal input signal, and A_0+a is the upper hard limit.

The n^{th} Fourier coefficient is calculated in Section II-B, and the results show that:

$$\begin{cases} A_{2n+1}=0 & n=0,1,2,\ldots \\ B_{2n}=0 & n=0,1,2,\ldots \end{cases} \tag{11}$$

The detailed calculation results are presented in Appendix A Table AII.

III. HOS Analysis

The definition of the HOS is introduced to analyze the harmonic characteristics of the nonlinear parts. The eigenfunction method is an important tool in statistical analysis since it can easily define the higher-order moments and cumulants.

The first joint eigenfunction of k continuous random variables $x_1,x_2,\ldots,x_k$ is defined as:

$$\begin{aligned} &\Phi(\omega_1,\omega_2,\ldots,\omega_k)\doteq E\left(\mathrm{e}^{\mathrm{j}(\omega_1x_1+\omega_2x_2+\ldots+\omega_kx_k)}\right)= \\ &\int_{-\infty}^{\infty}\ldots\int_{-\infty}^{\infty}f(x_1,x_2,\ldots,x_k)\mathrm{e}^{\mathrm{j}(\omega_1x_1+\omega_2x_2+\ldots+\omega_kx_k)}\mathrm{d}x_1\mathrm{d}x_2\ldots\mathrm{d}x_k \end{aligned} \tag{12}$$

where $f(\cdot)$ is the probability density function; and $E(\cdot)$ is the expectation function.

The k^{th}-order moment and cumulant of k random variables are obtained as:

$$E(x_1,x_2,\ldots,x_k)=(-\mathrm{j})^k\frac{\partial^k\Phi(\omega_1,\omega_2,\ldots,\omega_k)}{\partial\omega_1\partial\omega_2\ldots\partial\omega_k}\bigg|_{\omega_1=\omega_2=\ldots=\omega_k=0} \tag{13}$$

$$cum(x_1,x_2,\ldots,x_k)=(-\mathrm{j})^k\frac{\partial^k\ln\Phi(\omega_1,\omega_2,\ldots,\omega_k)}{\partial\omega_1\partial\omega_2\ldots\partial\omega_k}\bigg|_{\omega_1=\omega_2=\ldots=\omega_k=0} \tag{14}$$

For a stationary continuous random signal $x(t)$, we set $x_1 = x(t), x_2 = x(t+\tau_1), \ldots, x_k = x(t+\tau_{k-1})$, which are later substituted into (14). Consequently, the k^{th}-order cumulant of the random signal $x(t)$ is expressed as:

$$c_{kx}(\tau_1, \tau_2, \ldots, \tau_{k-1}) = cum\left(x(t), x(t+\tau_1), \ldots, x(t+\tau_{k-1})\right) \tag{15}$$

The k^{th}-order cumulant spectrum $S_{kx}(\cdot)$ is defined as the $(k-1)$-dimensional discrete Fourier transform of the k^{th}-order cumulant, which is expressed as:

$$S_{kx}(\omega_1, \omega_2, \ldots, \omega_{k-1}) = \sum_{\tau_1=-\infty}^{\infty} \cdots \sum_{\tau_{k-1}=-\infty}^{\infty} c_{kx}(\tau_1, \tau_2, \ldots, \tau_{k-1}) e^{-j(\omega_1\tau_1 + \omega_2\tau_2 + \ldots + \omega_{k-1}\tau_{k-1})} \tag{16}$$

Generally, a higher-order cumulant spectrum is referred to as a higher-order spectrum. Particularly, the third-order spectrum $S_{3x}(\omega_1, \omega_2)$ is referred to as the bi-spectrum because it is a two-frequency energy spectrum, which is represented by $B(\omega_1, \omega_2)$. Similarly, the fourth-order spectrum $S_{4x}(\omega_1, \omega_2, \omega_3)$ is referred to as the tri-spectrum, expressed as $T(\omega_1, \omega_2, \omega_3)$.

IV. Hard-Limiting DNB of VSC Control System

A. Modeling of VSC Control System

A typical direct-drive wind farm has 30-60 generators. Several direct-drive permanent magnet synchronous generators (PMSGs) are connected to form a string structure. The strings are further connected to a point of common coupling (PCC) and finally to the grid with a voltage level of 35 kV through a series of boosting transformers and transmission lines (equivalent to a set of impedances) [29], as shown in Fig. 3.

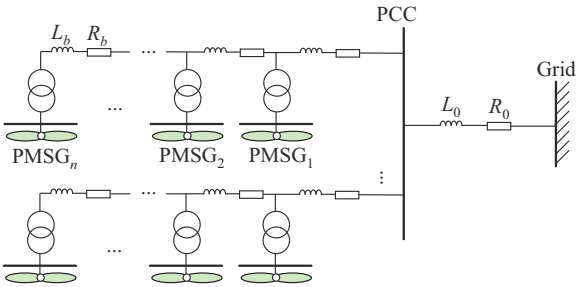

Fig. 3. Model of wind farm connected to grid.

Figure 4 shows the structure of a typical direct-drive wind generator. Because the machine-side converter adopts the maximum power tracking control, its interaction with the grid is limited. As presented in [30] and [31], the grid-related oscillation dynamics strongly depend on the DC capacitor and grid-side converter, and are slightly affected by the wind turbine, PMSG, and machine-side converter. Hence, the machine-side component, including the wind turbine, PMSG, and machine-side converter, is equivalent to a power source that outputs the power received by the wind turbine. Additionally, the grid-side converter is modeled as a VSC with its corresponding control system.

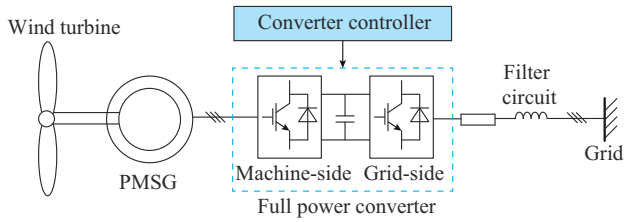

Fig. 4. Structure of a typical direct-drive wind generator.

Moreover, static reactive power compensation equipment, such as SVGs, is generally installed in wind farms. In this study, the SVG model adopts a double closed-loop control scheme. The *d*-axis control loop stabilizes the DC bus voltage, and the *q*-axis control loop varies based on the control mode. When the SVG operates in the constant-voltage control mode, the control target of the loop is the terminal voltage, and when it operates in the constant reactive power control mode, the control target of the loop is the output reactive power. Owing to its ability to produce high-quality output voltage waveforms with reduced harmonic distortion and low switching frequencies, many existing SVGs in wind farms are based on cascaded H-bridge topology [32], [33]. The average-value model that ignores the PWM dynamics and models the cascaded H-bridge in the circuit as a controlled voltage source is adopted in this study. Therefore, the SVG is modeled as a VSC with its corresponding control system.

Thus, we obtain a unified VSC control system for the PMSGs and SVGs in the wind farms. The only difference is the choice of control targets in the *d*- and *q*-axis control loops, as shown in Fig. 5. In this study, four hard limiters are considered as the nonlinear parts: two in the inner control loop of the current and two in the outer control loop of the voltage, respectively.

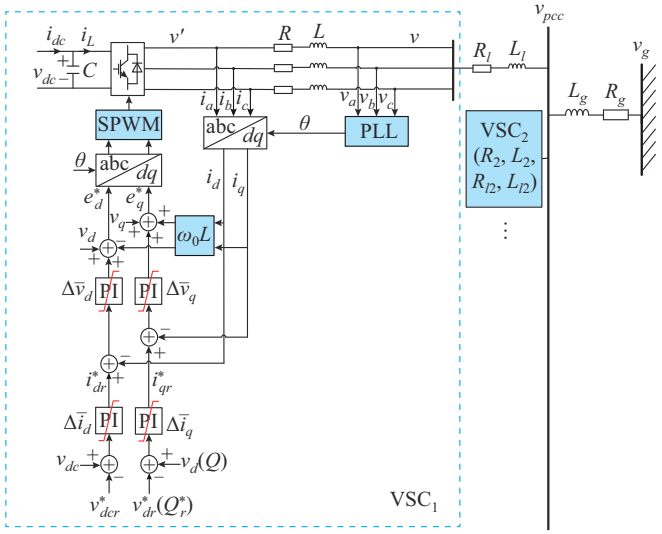

Fig. 5. Structure of VSC control system.

In Fig. 5, v_{dc} and v_{dcr}^* are the measured and reference DC bus voltages, respectively; C is the DC capacitor; v_d (or Q)

and v_{dr}^* (or Q_r^*) are the measured and reference d-axis terminal voltages (or the output reactive power), respectively; i_d and i_q are the d- and q-axis components of the output current of the VSC, respectively; e_d^* and e_q^* are the d- and q-axis components of the output voltage reference of the VSC, respectively; v', v, v_{pcc}, and v_g are the voltages of the VSC output, terminal, PCC, and grid, respectively; θ is the output angle of the phase-locked loop (PLL); and R, L and R_2, L_2 are the equivalent resistances and inductances of the transformer and transmission line between the VSC output and terminal, respectively; R_l, L_l and R_{l2}, L_{l2} are the equivalent resistances and inductances of the transmission line between the terminal and PCC, respectively; and R_g and L_g are the equivalent resistance and inductance of the transmission line between PCC and the grid, respectively.

B. Elimination of Effects from Linear Parts

While the nonlinear parts take effect inside the control system, the accident waveform record collected from the phasor measurement unit provides only voltage and current information at the terminal of the VSC. Hence, the relationship between the HOS of the hard-limit output and that of the terminal electrical quantities must be derived.

When the hard limiting in the d-axis inner control loop of the current takes effect, $\bar{v}_d$ is produced by the nonlinear part after proportional-integral (PI) control, as shown in Fig. 5. Assuming that the PLL performs satisfactorily and the VSC is synchronized with the system, the d-axis frame model of the main circuit is expressed as:

$$\Delta v_d' - \Delta v_d = (sL + R)\Delta i_d - \omega_0 L \Delta i_q \tag{17}$$

where Δ represents the small-signal perturbation; and ω_0 is the fundamental angular frequency.

Without considering the dynamics of the PWM, we assume that the VSC output tracks the reference signal:

$$\Delta v_d' = \Delta e_d^* \tag{18}$$

$$\Delta v_q' = \Delta e_q^* \tag{19}$$

From Fig. 5, the relationship between $\bar{v}_d$ and v_d' is obtained as:

$$\Delta v_d' = \Delta e_d^* = \Delta \bar{v}_d - \omega_0 L \Delta i_q + \Delta v_d \tag{20}$$

where $\bar{v}_d$ is the hard-limit output in the d-axis inner control loop of the current.

Then, we obtain the relationship between i_d and $\bar{v}_d$ by combining (17) and (20), as expressed below:

$$\Delta i_d = \frac{1}{sL + R}\Delta \bar{v}_d \tag{21}$$

Similarly, when the hard limiting in the q-axis inner control loop of the current takes effect, the relationship between i_q and $\bar{v}_q$ is expressed as:

$$\Delta i_q = \frac{1}{sL + R}\Delta \bar{v}_q \tag{22}$$

where $\bar{v}_q$ is the hard-limit output in the q-axis inner control loop of the current.

When the hard limit in the d-axis outer control loop of the voltage takes effect, the output $\bar{i}_d$ is produced by the nonlinear part after PI control. Thus, (20) can be rewritten as:

$$\Delta v_d' = G_i(s)\left(\Delta \bar{i}_d - \Delta i_d\right) - \omega_0 L \Delta i_q + \Delta v_d \tag{23}$$

where $\bar{i}_d$ is the output of the hard limit in the d-axis outer control loop of the voltage; and $G_i(s)$ is the transfer function of the inner control loop of the current.

Then, we obtain the relationship between i_d and $\bar{i}_d$ by combining (17) and (23), as expressed below:

$$\Delta i_d = \frac{G_i(s)}{sL + R + G_i(s)}\Delta \bar{i}_d \tag{24}$$

Similarly, when the hard limit in the q-axis outer control loop of the voltage takes effect, the relationship between i_q and $\bar{i}_q$ is expressed as:

$$\Delta i_q = \frac{G_i(s)}{sL + R + G_i(s)}\Delta \bar{i}_q \tag{25}$$

where $\bar{i}_q$ is the output of the hard limit in the q-axis outer control loop of the voltage.

Hence, the output of the nonlinear part in the control system can always be obtained from the current measured at the terminal after passing through the linear part by combining (21), (22), (24), and (25). The system shown in Fig. 6 illustrates how to eliminate the effects of the linear parts on HOS of the terminal current, wherein $e(n)$ and $y(n)$ are the input and output, respectively; and $H(z)$ represents the linear time-invariant part.

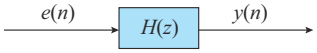

Fig. 6. Typical linear system.

The relationship between the HOS of $e(n)$ and that of $y(n)$ can be obtained based on the definition and properties of the HOS [34] as expressed below:

$$S_{ky}(\omega_1, \omega_2, \ldots, \omega_{k-1}) = S_{ke}(\omega_1, \omega_2, \ldots, \omega_{k-1}) H(\omega_1) \ldots H(\omega_{k-1}) H^*(\omega_1 + \omega_2 + \ldots + \omega_{k-1}) \tag{26}$$

where $S_{ke}(\omega_1, \omega_2, \ldots, \omega_{k-1})$ and $S_{ky}(\omega_1, \omega_2, \ldots, \omega_{k-1})$ are the k^{th}-order cumulant spectra of $e(n)$ and $y(n)$, respectively; $H(\omega)$ is the continuous transfer function of $H(z)$; and * is the conjugation operator. Let $k = 2, 3$ in (26). $S_2(\omega)$ is denoted by $P(\omega)$ and $S_3(\omega_1, \omega_2)$ is denoted by $B(\omega)$. Consequently, we can obtain:

$$P_y(\omega) = P_e(\omega)\left|H(\omega)\right|^2 \tag{27}$$

$$B_y(\omega_1, \omega_2) = B_e(\omega_1, \omega_2) H(\omega_1) H(\omega_2) H^*(\omega_1 + \omega_2) \tag{28}$$

Define $bic(\omega_1, \omega_2)$ as the bi-coherence [35] at the frequency pair (ω_1, ω_2), which is calculated as:

$$bic(\omega_1, \omega_2) = \left| \frac{B(\omega_1, \omega_2)}{\sqrt{P(\omega_1) P(\omega_2) P(\omega_1 + \omega_2)}} \right| \tag{29}$$

By combining (27), (28), and (29), we can obtain:

$$bic_y(\omega_1, \omega_2) = bic_e(\omega_1, \omega_2) \tag{30}$$

Further, we define the tri-coherence $tric(\omega_1, \omega_2, \omega_3)$ [35] as:

$$tric(\omega_1,\omega_2,\omega_3)=\frac{\left|T(\omega_1,\omega_2,\omega_3)\right|}{\sqrt{P(\omega_1+\omega_2+\omega_3)P(\omega_1)P(\omega_2)P(\omega_3)}} \tag{31}$$

Similarly, it can be proven that $tric_y(\omega_1,\omega_2,\omega_3)=tric_e(\omega_1,\omega_2,\omega_3)$.

Consequently, the linear part does not change the bi- or tri-coherence of the system. Obtaining the waveforms of i_d and i_q at the terminal of the VSC and performing the HOS analysis enable the detection of the nonlinearity of the VSC system.

C. Bi-coherence Spectrum and Uni-lateral Saturation Hard-limiting Detection

Based on the results in Section II-C, when a self-sustained oscillation occurs, the output of the uni-lateral saturation hard limiter contains the second harmonic of the oscillation frequency with the same phase as that of the fundamental frequency. Without loss of generality, let its initial phase be zero, i.e.,

$$y(t)=B_1\sin 2\pi ft+B_2\sin(2\pi\times 2ft) \tag{32}$$

where f denotes the oscillation frequency; and B_1 and B_2 are the coefficients of the fundamental and second Fourier harmonics, respectively.

A Fourier transform is performed twice on the second-order autocorrelation function of $y(t)$. Consequently, the bi-spectrum of $y(t)$ can be expressed as:

$$B_y(\omega_1,\omega_2)=\int_{-\infty}^{\infty}\int_{-\infty}^{\infty}f\int_0^{1/f}y(t)\,y(t+\tau_1)\,y(t+\tau_2)\,\mathrm{d}t\cdot \mathrm{e}^{-\mathrm{j}2\pi(\omega_1+\omega_2)}\mathrm{d}\tau_1\,\mathrm{d}\tau_2 \tag{33}$$

The bi-spectrum has 12 symmetrical regions [35], as shown in Fig. 7(a).

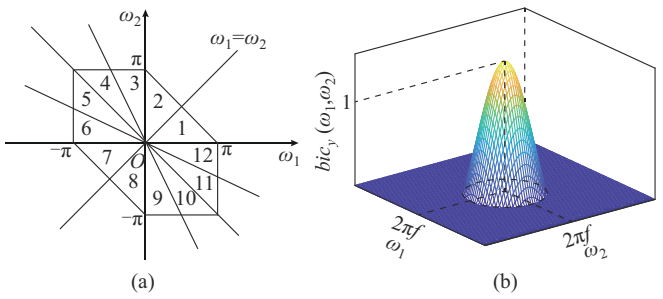

(a) (b)

Fig. 7. Related figures of bi-spectrum and bi-coherence spectrum. (a) Symmetric region of bi-spectrum. (b) Peak of bi-coherence spectrum.

Therefore, to completely describe the entire bi-spectrum, only a symmetrical region in the resulting $B_y(\omega_1,\omega_2)$ is required for analysis. Considering $\{(\omega_1,\omega_2)|0\le\omega_1\le\omega_2\}$, $B_y(\omega_1,\omega_2)$ can be calculated as:

$$B_y(\omega_1,\omega_2)=\frac{\pi}{4}\mathrm{j}B_1^2B_2\delta(\omega_1-2\pi f)\delta(\omega_2-2\pi f) \tag{34}$$

where $\delta(\cdot)$ is the Dirac delta function [36], which is expressed as:

$$\begin{cases}\delta(x)=0 & x\ne 0\\ \int_{-\infty}^{\infty}\delta(x)\,\mathrm{d}x=1\end{cases} \tag{35}$$

where $\delta(x)$ is a finite maximum at $x=0$ when the input signal is discretized. In (34), $B_y(\omega_1,\omega_2)$ is a finite maximum if and only if $\omega_1=\omega_2=2\pi f$; otherwise, it is zero. Therefore, a peak can be observed at the x-y coordinates $(2\pi f,2\pi f)$ in the three-dimensional (3D) graph of $\{(\omega_1,\omega_2,B_y(\omega_1,\omega_2))|0\le\omega_1\le\omega_2\}$. Furthermore, because $(2\pi f,2\pi f)$ is on the symmetry axis $\omega_1=\omega_2$, when the area is extended to $\{(\omega_1,\omega_2)|\omega_1\ge 0,\omega_2\ge 0\}$ (areas 1 and 2 in Fig. 7(a)), the peak at $(2\pi f,2\pi f)$ still exists.

The power spectrum of $y(t)$ is derived as:

$$P_y(\omega)=\int_{-\infty}^{\infty}f\int_0^{1/f}y(t)\,y(t+\tau)\,\mathrm{d}t\cdot\mathrm{e}^{-\mathrm{j}2\pi\omega}\mathrm{d}\tau=\frac{1}{2}B_1^2\sqrt{\frac{\pi}{2}}\delta(\omega-2\pi f)+\frac{1}{2}B_2^2\sqrt{\frac{\pi}{2}}\delta(\omega-4\pi f) \tag{36}$$

Based on (29), (34), and (36), the bi-coherence spectrum $(\{(\omega_1,\omega_2)|\omega_1\ge 0,\omega_2\ge 0\})$ can be calculated as:

$$bic_y(\omega_1,\omega_2)=\frac{\left|B_y(\omega_1,\omega_2)\right|}{\sqrt{P_y(\omega_1+\omega_2)P_y(\omega_1)P_y(\omega_2)}}=\frac{\frac{\pi}{4}B_1^2B_2\delta(\omega_1-2\pi f)\delta(\omega_2-2\pi f)}{\sqrt{\frac{1}{2}B_1^2\sqrt{\frac{\pi}{2}}\delta(\omega_1-2\pi f)+\frac{1}{2}B_2^2\sqrt{\frac{\pi}{2}}\delta(\omega_1-4\pi f)}\sqrt{\frac{1}{2}B_1^2\sqrt{\frac{\pi}{2}}\delta(\omega_2-2\pi f)+\frac{1}{2}B_2^2\sqrt{\frac{\pi}{2}}\delta(\omega_2-4\pi f)}\sqrt{\frac{1}{2}B_1^2\sqrt{\frac{\pi}{2}}\delta(\omega_1+\omega_2-2\pi f)+\frac{1}{2}B_2^2\sqrt{\frac{\pi}{2}}\delta(\omega_1+\omega_2-4\pi f)}}\quad \omega_1\ge 0,\omega_2\ge 0 \tag{37}$$

Since $\mathbb{F}^{-1}(\delta(\omega))=\frac{1}{\sqrt{2\pi}}$, it can be proven that the bi-coherence spectrum of $y(t)$ reaches its peak if and only if $\omega_1=\omega_2=2\pi f$, as shown in Fig. 7(b). It is further calculated as:

$$bic_y(2\pi f,2\pi f)=\frac{\frac{\pi}{4}B_1^2B_2\frac{1}{\sqrt{2\pi}}\frac{1}{\sqrt{2\pi}}}{\sqrt{\frac{1}{2}B_1^2\sqrt{\frac{\pi}{2}}\frac{1}{\sqrt{2\pi}}\frac{1}{2}B_1^2\frac{1}{\sqrt{2\pi}}\sqrt{\frac{\pi}{2}}\frac{1}{2}B_2^2\frac{1}{\sqrt{2\pi}}\sqrt{\frac{\pi}{2}}}}=1 \tag{38}$$

In (35), $bic_y(\omega_1,\omega_2)\ge 0$. Therefore, the range of the corresponding bi-coherence value of each x-y coordinate in the bi-coherence spectrum is $[0,1]$. The larger the bi-coherence value, the stronger the nonlinear phase coupling between the two frequencies corresponding to the coordinate (the stron-

ger the nonlinearity).

In (32), when $y(t)$ extends to $y(t)=\sum_{n=1}^{+\infty}B_n\sin(2\pi nft)$, it can be proven that in the 3D graph of $\left\{\left(\omega_1,\omega_2,bic_y(\omega_1,\omega_2)\right)\middle|\omega_1\geq 0,\omega_2\geq 0\right\}$, there are peaks at the *x*-*y* coordinates $\left(i\cdot 2\pi f,j\cdot 2\pi f\right)(i,j=1,2,3,\ldots)$, and their corresponding bi-coherence values are equal to one. Furthermore, it can be proven that the conclusion remains unchanged when $y(t)=\sum_{n=1}^{+\infty}A_{2n}\cos\left(2\pi\times 2nft\right)+\sum_{n=0}^{+\infty}B_{2n+1}\sin\left(2\pi(2n+1)ft\right)$, which accurately represents the output of the uni-lateral saturation hard limiter according to (11).

D. Tri-coherence Spectrum and Bi-lateral Saturation Hard-limiting Detection

Based on the results in Section II-B, when $y(t)=\sum_{n=0}^{+\infty}B_{2n+1}\sin\left(2\pi(2n+1)ft\right)$, which accurately represents the output of the bi-lateral saturation hard limiter according to (9), it can be proven that in the 4D graph of $\left\{\left(\omega_1,\omega_2,\omega_3,tric_y(\omega_1,\omega_2,\omega_3)\right)\middle|\omega_1\geq 0,\omega_2\geq 0,\omega_3\geq 0\right\}$, peaks exist at the *x*-*y*-*z* coordinates $\left((2i+1)\times 2\pi f,(2j+1)\times 2\pi f,(2k+1)\times 2\pi f\right)(i,j,k=0,1,2,\ldots)$, with the peak values of 1. The range of the corresponding tri-coherence value of each *x*-*y*-*z* coordinate in the tri-coherence spectrum is $[0,1]$. Furthermore, the larger the tri-coherence value, the stronger the nonlinear phase coupling among the three frequencies corresponding to the coordinate (the stronger the nonlinearity).

The detailed derivation process is presented in Appendix B.

E. Nonlinearity Detection and Classification of VSC Control Systems

Based on Section IV-B, the nonlinearity induced by hard limiting in the VSC control system can be detected by transforming the current waveform into i_d and i_q at the terminal of the VSC and performing the HOS (bi-/tri-coherence) analysis. The nonlinearity of i_d represents the nonlinearity in the *d*-axis control loop of the VSC control system, whereas the nonlinearity of i_q represents the nonlinearity in the *q*-axis.

Table I summarizes the results obtained in Sections IV-C and IV-D. By examining the relationship between the peak coordinates of the HOS and harmonic characteristics of the analyzed signal, the bi-coherence spectrum is used to detect the "phase coupling". Thus, the harmonics with frequencies $f_1+f_2=f_3$ and phases $\varphi_1+\varphi_2=\varphi_3$ are simultaneously satisfied. Furthermore, the tri-coherence spectrum is used to detect whether $f_1+f_2+f_3=f_4$ and $\varphi_1+\varphi_2+\varphi_3=\varphi_4$ are both satisfied. It is noteworthy that the phase equation is sufficient but unnecessary in the phase coupling phenomenon, which is thoroughly explained in Section VI-A.

Table I shows that the output of the uni-lateral saturation hard limiter contains harmonics of all orders and satisfies both the quadratic and cubic phase coupling. Thus, peaks exist both in the bi- and tri-coherence spectra. Hence, the bi-coherence spectrum must be first examined, followed by the tri-coherence spectrum. Nonlinearity can be assessed and classified, as shown in Fig. 8.

TABLE I
CHARACTERISTICS OF BI-COHERENCE AND TRI-COHERENCE SPECTRA

Type	Phase coupling	Uni-lateral saturation	Bi-lateral saturation
Fourier series		$y(t)=\sum_{n=1}^{+\infty}A_{2n}\cos\left(2\pi\times 2nft\right)+\sum_{n=0}^{+\infty}B_{2n+1}\sin\left(2\pi(2n+1)ft\right)$	$y(t)=\sum_{n=0}^{+\infty}B_{2n+1}\sin\left(2\pi(2n+1)ft\right)$
Bi-coherence	$f_1+f_2=f_3,\varphi_1+\varphi_2=\varphi_3$	Peaks	No peaks
Tri-coherence	$f_1+f_2+f_3=f_4,\varphi_1+\varphi_2+\varphi_3=\varphi_4$	Peaks	Peaks

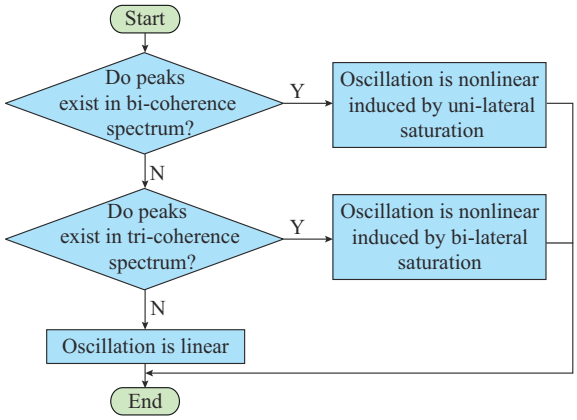

Fig. 8. Flowchart of nonlinearity detection and classification.

In this study, when detection is performed at the VSC terminal, only hard limiting related nonlinearity exists in the control system (average-value model), and all the other function blocks in the control system can be represented by the transfer functions (linear blocks). Therefore, we assume that hard limiting is the only source of nonlinearity in Fig. 8.

V. PROCEDURE FOR HARD-LIMITING DNB OF VSC CONTROL SYSTEM

The specific procedure for applying the hard-limiting DNB to the VSC control system is based on the theoretical analysis described in Section IV. The corresponding steps are summarized in Fig. 9, and the detailed process is as follows.

To obtain the time series for the calculation, we first collect the accident waveform records of the current at the terminal of the VSC. The studied signals $x_a(k)$, $x_b(k)$, and $x_c(k)$ are sampled from the three-phase currents $i_a(t)$, $i_b(t)$, and $i_c(t)$, respectively. We begin the sampling from the ini-

tial time t_0 and set the sampling interval to Δt. The sampling point is denoted by k, and the sample length is L, i.e.,

$$\begin{cases} x_a(k) = i_a(t_0 + k\Delta t) \\ x_b(k) = i_b(t_0 + k\Delta t) \quad k = 1, 2, \ldots, L \\ x_c(k) = i_c(t_0 + k\Delta t) \end{cases} \tag{39}$$

Step	Points
Preparation	Obtain the time series for the calculation sampling from the accident waveform records
Step 1-Step 3	Pretreatments: *dq* transformation and division of segments
Step 4-Step 7	Windowing and FFT: reduction of leakage errors treatment of 0/0
Step 8-Step 11	Calculation of spectrum: eliminate the effects of random phases
Step 12	Determination of DNB thresholds: peak value and flatness
Step 13	Selection of *d*- and *q*-axis

Fig. 9. Key points of procedure for hard-limiting DNB.

Step 1: perform a *dq* transformation on the three-phase sampling signals $x_a(k)$, $x_b(k)$, and $x_c(k)$. The initial phase θ_0 can be obtained by applying a PLL algorithm as expressed below:

$$\begin{bmatrix} x_d(k) & x_q(k) & x_0(k) \end{bmatrix}^{\mathrm{T}} = \frac{2}{3} \begin{bmatrix} \cos(\theta(k) + \theta_0) & \cos\left(\theta(k) - \frac{2}{3}\pi\right) & \cos\left(\theta(k) + \frac{2}{3}\pi\right) \\ -\sin(\theta(k) + \theta_0) & -\sin\left(\theta(k) - \frac{2}{3}\pi\right) & -\sin\left(\theta(k) + \frac{2}{3}\pi\right) \\ \frac{1}{2} & \frac{1}{2} & \frac{1}{2} \end{bmatrix} \cdot \begin{bmatrix} x_a(k) & x_b(k) & x_c(k) \end{bmatrix}^{\mathrm{T}} \tag{40}$$

where $\theta(k) = \omega_0 k\Delta t + \theta_0$; and $x_d(k)$, $x_q(k)$, and $x_0(k)$ are the transformation results in the *dq*0 coordinate system.

Step 2: set the transformation result $x_d(k)$ of the previous step as the subsequent signal processing object, i.e.,

$$x(k) = x_d(k) \tag{41}$$

Step 3: divide $x(k)$ into M segments, wherein each segment length is N ($MN = L$). Each segment is recorded as $x^{(i)}(l)$ ($i = 1, 2, \ldots, M$; $l = 1, 2, \ldots, N$).

Step 4: select an appropriate window function, such as a Hanning window, which is expressed as:

$$w(l) = \frac{1}{2}\left(1 + \cos\left(2\pi \frac{l}{N-1}\right)\right) \tag{42}$$

Multiply each segment of the signal by the window function, and use the obtained results $x'^{(i)}(l)$ for further calculations to reduce leakage errors, as expressed below:

$$x'^{(i)}(l) = x^{(i)}(l) w(l) \tag{43}$$

Step 5: for each segment $x'^{(i)}(l)$, subtract its mean value as:

$$\hat{x}^{(i)}(l) = x'^{(i)}(l) - \bar{x}^{(i)}(l) \tag{44}$$

Step 6: perform the fast Fourier transform (FFT) on each segment $\hat{x}^{(i)}(l)$:

$$X_k^{(i)} = \frac{1}{N}\sum_{l=1}^{N} \hat{x}^{(i)}(l) \mathrm{e}^{-i \cdot 2\pi kl/N} \quad k = 1, 2, \ldots, N/2, i = 1, 2, \ldots, M \tag{45}$$

Step 7: when dealing with the FFT results, consider a small parameter σ (for instance, $\sigma = 0.001$). Sweep $i = 1, 2, \ldots, M$, and for any k, if $X_k^{(i)} < \sigma \max\limits_{k=1,2,\ldots,N/2} X_k^{(i)}$, then let $X_k^{(i)} = \sigma^2 \max\limits_{k=1,2,\ldots,N/2} X_k^{(i)}$. This step can further increase the difference in the order of magnitudes between the white noise and peak value in the spectrum. Thus, the analysis and conclusion of the peak value is not affected by the appearance of the values close to 0/0 in the bi- and tri-coherence spectrum.

Step 8: the estimated values of the power spectrum, bi-spectrum, and tri-spectrum of $x(k)$ are expressed as:

$$\hat{P}(m) = \frac{1}{M}\sum_{i=1}^{M} X_m^{(i)} X_m^{*(i)} \tag{46}$$

$$\hat{B}(m,n) = \frac{1}{M}\sum_{i=1}^{M} X_m^{(i)} X_n^{(i)} X_{m+n}^{*(i)} \tag{47}$$

$$\hat{T}(m,n,o) = \frac{1}{M}\sum_{i=1}^{M} X_m^{(i)} X_n^{(i)} X_o^{(i)} X_{m+n+o}^{*(i)} \tag{48}$$

Step 9: calculate the bi-coherence spectrum as:

$$\hat{bic}(m,n) = \frac{\left|\hat{B}(m,n)\right|}{\sqrt{\hat{P}(m+n)\hat{P}(m)\hat{P}(n)}} \tag{49}$$

Step 10: the obtained bi-coherence spectrum is a 3D graph. Its *x*-*y* coordinates are the (m,n) frequencies and its *z* coordinate is the corresponding bi-coherence value, whose theoretical value range is $[0, 1]$.

Step 11: calculate the tri-coherence spectrum as:

$$\hat{tric}(m,n,o) = \frac{\left|\hat{T}(m,n,o)\right|}{\sqrt{\hat{P}(m+n+o)\hat{P}(m)\hat{P}(n)\hat{P}(o)}} \tag{50}$$

Step 12: determination of DNB thresholds.

Peak value threshold: define σ_p as the nonlinear threshold (preferably 0.3). A peak in the bi- or tri-coherence spectrum whose value is greater than σ_p is considered to characterize the existence of the quadratic or cubic phase coupling, and the coordinates of the peak represent the corresponding frequencies. The conclusion and classification of the nonlinearity can be completed using the process provided in Fig. 8.

Flatness threshold: in addition to the index σ_p for checking the peak values, a nonlinear index μ can be defined based on the graph flatness [37] for the bi-coherence spectrum:

$$\mu \triangleq \left| \hat{bic}^2_{\max} - \left(\overline{\hat{bic}}^{\,2} + 2\sigma_{\hat{bic}^2} \right) \right| \tag{51}$$

where $\overline{\hat{bic}}^{\,2}$ is the average of the estimated squared bi-coher-

ence; and $\sigma_{\hat{bic}^2}$ is the standard deviation of $\hat{bic}^2$. Based on the power-quality standard [38], the corresponding result of the index μ is 0.0180 for 35 kV networks obtained by simulation, while considering the measurement of the output currents with the background harmonics. Consequently, we set the threshold $\mu_p=0.10$ to keep a sufficient margin. Here, the nonlinear behavior is considered existent if $\mu>\mu_p$.

For a single VSC with slight harmonic pollution, the peak value threshold is enough for the DNB. Contrarily, for the multi-VSCs or complex systems, the flatness threshold can be considered. However, only the existence of nonlinear behavior in the control system can be verified, and misjudgment may occur when using the flatness threshold to locate the nonlinear oscillatory source, which is illustrated and discussed in Section VI-C.

Step 13: the above steps implement the DNB on the *d*-axis control loop of the VSC control system. To study the *q*-axis control loop, return to *Step 2*: let $x(k)=x_q(k)$ and repeat *Steps 3-12*.

Consequently, the nonlinear behavior caused by the bi- or uni-lateral saturation hard limiting in the *d*- or *q*-axis control loop can be detected. Some of these steps increase the resolution and effectiveness of the HOS. *Step 4* reduces the spectrum leakage, *Steps 6* and *8* eliminate the effect of the random phases, and *Step 7* adds credibility to the presence of peaks.

VI. Case Studies

Three cases are presented and discussed to evaluate the effectiveness of the proposed method for the hard-limiting DNB in the VSC control system.

Case 1 considers an artificially constructed signal that is abstracted from the harmonic characteristics of the uni-lateral saturation hard limiter in Section II-C to further demonstrate whether $\varphi_1+\varphi_2=\varphi_3$ is a necessary condition of phase coupling in HOS.

Case 2 sets up a grid-connected PMSG model to demonstrate the effectiveness of the proposed process in detecting the nonlinearity owing to the uni-lateral saturation hard limiting by collecting accident waveform records at the terminals of the VSCs. In this case, the nonlinearity owing to bi-lateral saturation hard limiting is also detected later using the tri-coherence spectrum.

Case 3 sets up an IEEE 9-bus system with three SVGs and one static VAR compensator (SVC), wherein the self-sustained oscillation is induced by two SVGs. This case shows that the HOS can only detect the presence of nonlinearity but not locate the source of the nonlinear oscillations.

A. Case 1

Here, the following signal is considered in MATLAB.

$$x(n)=\cos\left(2\pi f_1 n/f_s+\varphi_1+w_1(n)\right)+\cos\left(2\pi f_2 n/f_s+\varphi_2+w_2(n)\right)+\cos\left(2\pi f_3 n/f_s+\varphi_3+w_3(n)\right) \tag{52}$$

where $f_1=0.6381$ Hz; $f_2=0.8345$ Hz; $f_3=f_1+f_2$; f_s is the sampling frequency; and $w_i(n)$ $(i=1,2,3)$ is a –20 dB Gaussian white noise.

In (52), let $\varphi_1=\varphi_2=\varphi_3=0$, and record $x(n)$ as $x_1(n)$. Further, let $\varphi_1=\varphi_2=0$, $\varphi_3=\pi/2$, and record $x(n)$ as $x_2(n)$.

Figure 10(a) shows the frequency spectrum of $x_1(n)$, from which three frequency components f_1, f_2, and f_3 can be found. However, the relationship between them cannot be determined. Figure 10(b) shows the bi-coherence spectrum of $x_1(n)$ as a contour map. Its peak appears at (f_1, f_2) and (f_2, f_1), with a peak value of 1.0. Hence, the power at f_3 comes entirely from the quadratic phase coupling of f_1 and f_2, which confirms the conclusion in Section IV-C. Figure 10(c) and (d) shows the frequency and bi-coherence spectrum of $x_2(n)$, which are almost the same as those in Fig. 10(a) and (b), respectively. However, in our initial setting, $\varphi_1+\varphi_2=\varphi_3$ in $x_1(n)$, whereas $\varphi_1+\varphi_2\neq\varphi_3$ in $x_2(n)$.

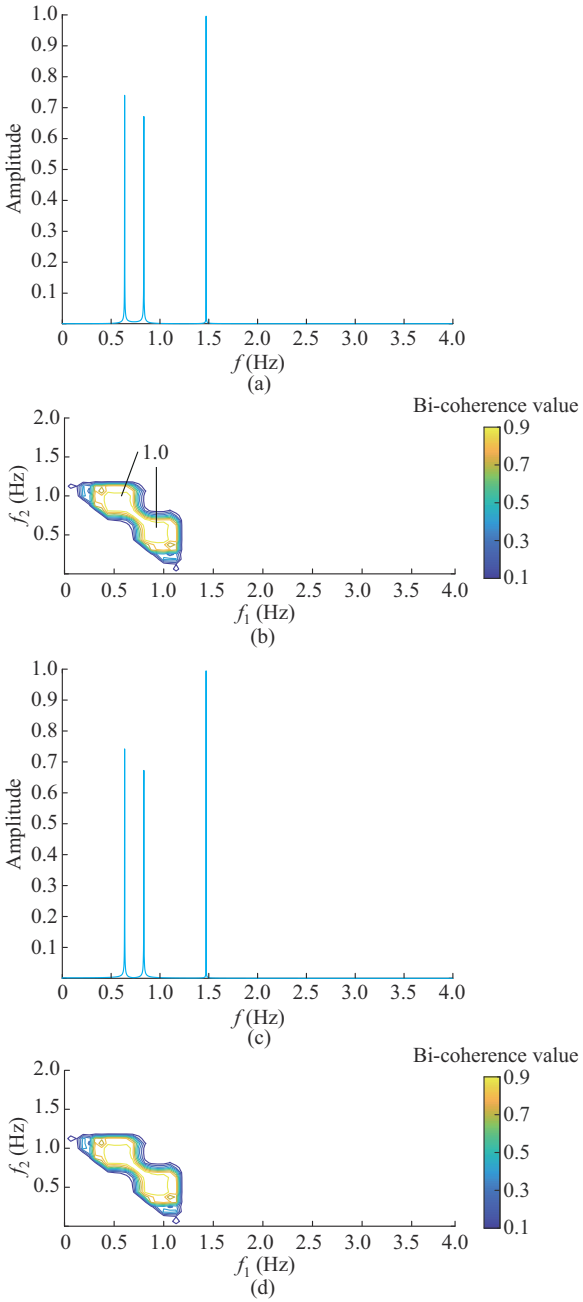

Fig. 10. Detection of quadratic phase coupling. (a) Frequency spectrum of $x_1(n)$. (b) Bi-coherence spectrum of $x_1(n)$. (c) Frequency spectrum of $x_2(n)$. (d) Bi-coherence spectrum of $x_2(n)$.

Previous studies [39] - [41] considered a quadratic phase coupling which is equivalent to $f_1+f_2=f_3$ and $\varphi_1+\varphi_2=\varphi_3$. In this case, when the condition extends to "$\varphi_1+\varphi_2-\varphi_3$ is constant", the phase coupling phenomenon and the peaks will also exist in the bi-coherence spectrum. Therefore, the phase equation is a sufficient but not unnecessary condition.

In this study, according to (11), the output of the uni-lateral saturation hard limiter can be expressed as:

$$y(t)=\sum_{n=1}^{+\infty}A_{2n}\cos\left(2\pi\times 2nft\right)+\sum_{n=0}^{+\infty}B_{2n+1}\sin\left(2\pi(2n+1)ft\right)=\sum_{n=1}^{+\infty}A_{2n}\sin\left(2\pi\times 2nft+\frac{\pi}{2}\right)+\sum_{n=0}^{+\infty}B_{2n+1}\sin\left(2\pi(2n+1)ft\right) \tag{53}$$

Therefore, the peaks with values greater than σ_p will appear in its bi-coherence spectrum similarly to a "chessboard" because any two integer multiples of the fundamental frequency have the property of the quadratic phase coupling. However, if the bi-coherence could detect only those satisfying $f_1+f_2=f_3$ and $\varphi_1+\varphi_2=\varphi_3$ simultaneously, no peaks in the bi-coherence spectrum will exist, which does not match the actual situation.

B. Case 2

A detailed grid-connected PMSG model is set up in PSCAD/EMTDC with the structure of the VSC control system shown in Fig. 11.

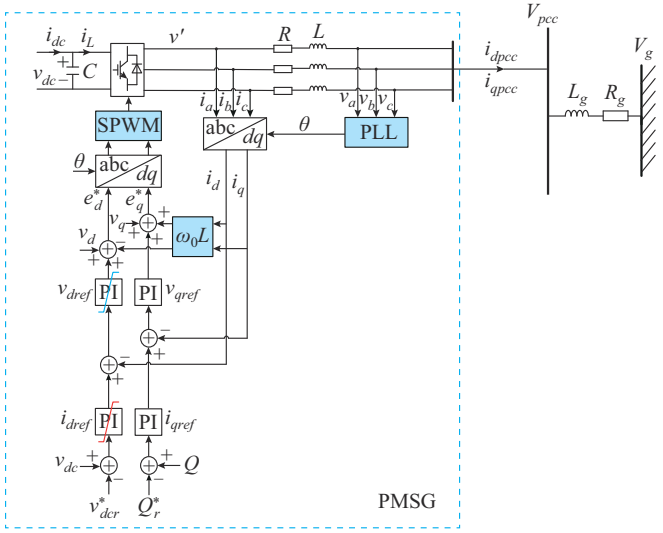

Fig. 11. PMSG model for DNB.

First, the parameters are adjusted to make the hard limit of PI in the *d*-axis outer control loop of the voltage take effect. Table II presents the parameter settings.

The simulation is implemented as follows.

$t=0$ s: use a voltage source to charge the DC capacitor. In the initial state, the PMSG is off-grid, and the active power and reactive power references are both zero.

$t=0.2$ s: the DC capacitor side is switched to the power source, and the PMSG is connected to the grid.

$t=1.0$ s: the active power is set to be 0.34 MW.

$t=2.0$ s: $G_i(s)$ is set to be $0.2+20/s$.

TABLE II
PARAMETERS IN CONTROL BLOCKS OF PMSG

Symbol	Description	Value
V_g	Grid voltage	0.69 kV
f_0	Fundamental frequency	50 Hz
P_N	Rated capacity of PMSG	1.5 MW
$H_{PLL}(s)$	PLL	$500+900/s$
P	Active power	0.34 MW
C	DC capacitor	200 mF
R	Connection resistance	0.001 Ω
L	Connection inductance	0.35 mH
R_g	Grid-side resistance	0.005 Ω
L_g	Grid-side inductance	0.4 mH
$G_{dc}(s)$	DC-voltage controller	$9+500/s$
$G_q(s)$	Reactive power controller	$0.3+50.28/s$
$G_i(s)$	Inner-loop current controller	$0.012+12.5/s$

$t=4.0$ s: $G_i(s)$ is set to be $0.012+12.5/s$.

Figure 12 shows the *d*-axis current reference i_{dref}. According to Fig. 12, the oscillation can be divided into two stages.

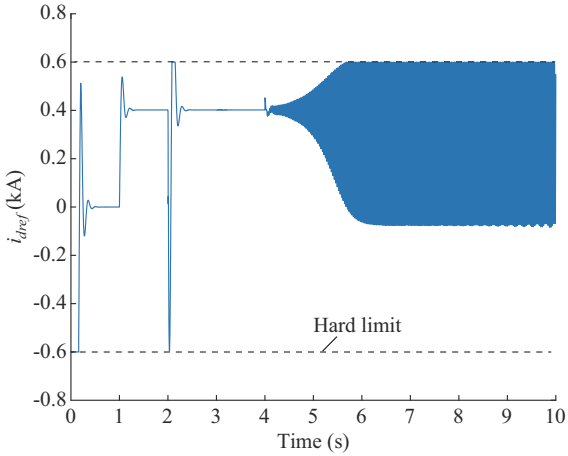

Fig. 12. *d*-axis current reference.

Stage I: after $t=4.0$ s and before any hard limit takes effect, the system can be analyzed with small-signal linearization. Based on the parameters presented in Table II, the dominating mode of the system state space model is $6.32\pm$ j190.06, which is on the right side of the imaginary axis. It induces a divergent oscillation and activates the hard limits of PI.

Stage II: after the oscillation causes i_{dref} to reach the hard limit of PI in the *d*-axis outer control loop of the voltage, the hard limit becomes uni-laterally saturated and the system cannot be analyzed by the linearization method. At the PCC, a constant-amplitude self-sustained oscillation of 33.8 Hz is observed, as shown in Fig. 13. The oscillating frequency can be computed and examined using the DF-based Nyquist criterion [13]. Since the transient process is short, the collected accident waveform record may only contain the constant-amplitude part, which superficially resembles a weakly-damped linear oscillation.

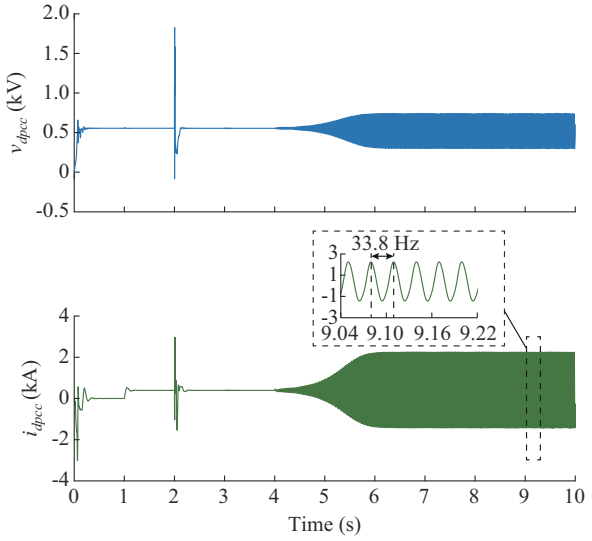

Fig. 13. Voltage and current at PCC in *d*-axis.

Figure 14 shows the bi-coherence and power spectra of i_{dref} and i_{dpcc}. The bi-coherence spectra are shown as contour maps whose *x*-*y* axis range is restricted to $\{(f_1,f_2)|\omega_1 \geq 0, \omega_2 \geq 0\}$, respectively. As shown in Fig. 14(a), the bi-coherence spectrum of i_{dref} resembles a "chessboard". Hence, the quadratic phase coupling exists between any two integer multiples of the fundamental frequency. Generally, the transfer function of the VSC control system is low-pass, which can be observed by comparing Fig. 14(b) and (d). However, the bi-coherence spectrum of i_{dpcc} can still maintain the property of the quadratic phase coupling, as shown in Fig. 14(c). Here, the peaks of the higher harmonics disappear because their amplitudes are too small to maintain a distinction from the background noise. Hence, Fig. 14(c) confirms that nonlinearity owing to uni-lateral saturation hard limit can be detected by collecting accident waveforms at the terminal of VSCs based on the HOS analysis. In this case, nonlinearity exists in the *d*-axis control loop of the VSC system.

Next, we adjust the parameters to examine the effectiveness of the tri-coherence spectrum. We set the upper and lower limits of the *d*-axis current reference i_{dref} to $\pm\infty$ and set those of the *d*-axis voltage reference v_{dref} to ± 0.08. Then, the hard limit of v_{dref} takes effect and induces a bi-lateral saturation self-sustained oscillation.

Figure 15(a) shows the bi-coherence spectrum of i_{dpcc}, with a global maximum value of only 0.002134, which is much smaller than the nonlinear threshold σ_p. Consequently, we consider that no peaks representing the nonlinearity exist in the contour map and no uni-lateral saturation exists.

Figure 15(b) shows the tri-coherence spectrum of i_{dpcc}, with a peak at the *x*-*y*-*z* coordinates (33.8 Hz, 33.8 Hz, 33.8 Hz). Here, the aliasing error expands the peak range, thereby making the maximum value larger than one; however, it still demonstrates the bi-lateral saturation in the system, which proves the effectiveness of the calculation and classification processes proposed in Section IV-E and Section V.

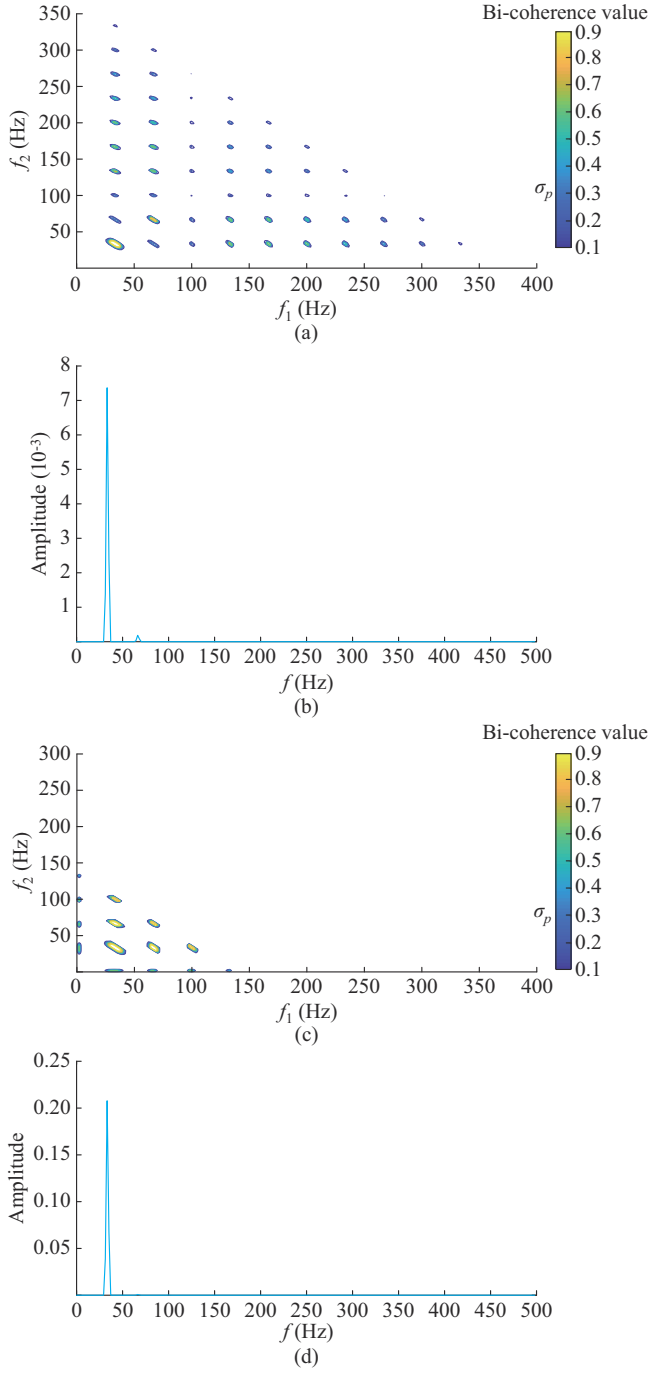

Fig. 14. Bi-coherence and power spectra of i_{dref} and i_{dpcc}. (a) Bi-coherence spectrum of i_{dref}. (b) Power spectrum of i_{dref}. (c) Bi-coherence spectrum of i_{dpcc}. (d) Power spectrum of i_{dpcc}.

C. Case 3

Figure 16 illustrates a topology derived from the IEEE 9-bus system, wherein the network parameters of buses 1-9 correspond with the IEEE 9-bus system. Contrary to the IEEE benchmark system, an SVC is located at the medium-voltage bus 13 for reactive power adjustment, and two grid-connected wind farms and their corresponding SVGs are located at buses 14 and 15. The PMSGs and SVGs use the double-loop VSC control, as presented in Section IV-A. The control parameters are presented in Table III.

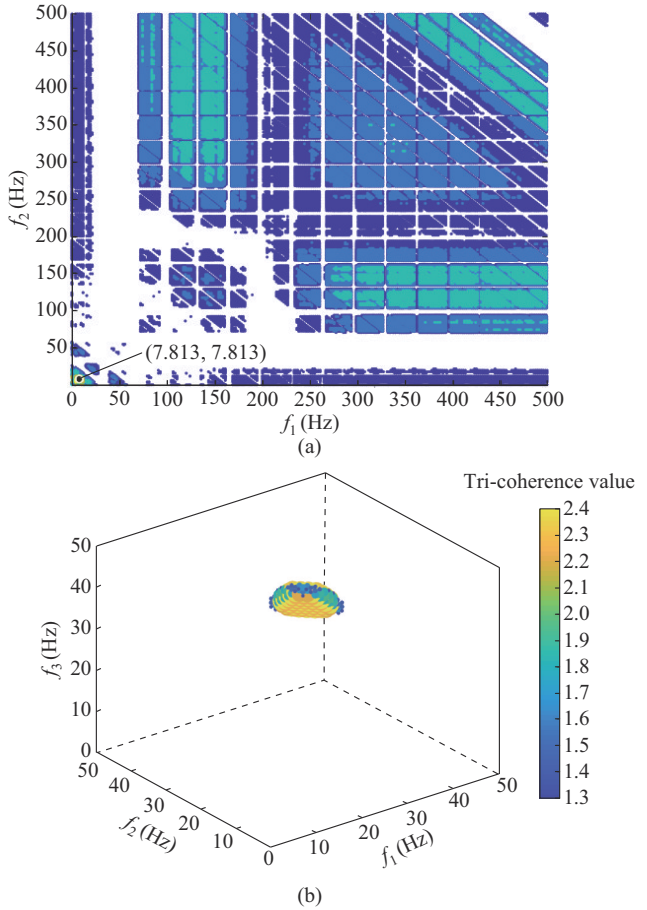

Fig. 15. Bi- and tri-coherence spectra of i_{dpcc}. (a) Bi-coherence spectrum of i_{dpcc}. (b) Tri-coherence spectrum of i_{dpcc}.

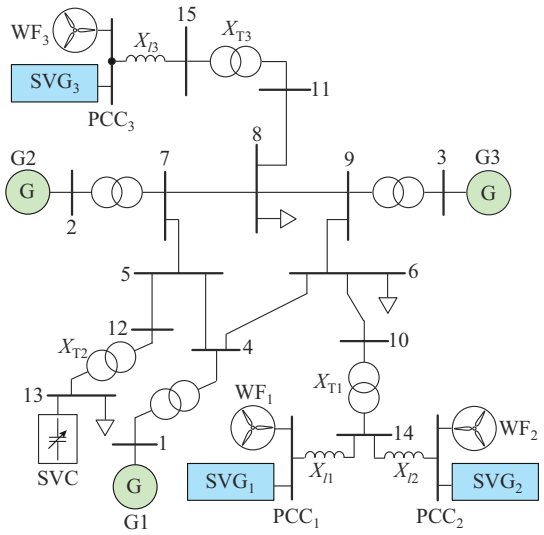

Fig. 16. Topology of case study system.

The case study system is simulated using PSCAD/EMTDC. In the case, a self-sustained oscillation is induced by mismatching the reference terminal voltages of SVG_1 and SVG_2, which are denoted by V_{ref1} and V_{ref2}, respectively. Figure 17 shows the oscillation-related waveforms of the voltages and currents. In Fig. 17(a), when $t<2$ s, set $V_{ref1}=V_{ref2}=1.005$ p.u., thereby stabilizing the voltage amplitudes V_{14}, V_{pcc1}, and V_{pcc2}. Contrarily, when $t\geq 2.45$ s, set $V_{ref1}=1.005$ p.u. and $V_{ref2}=1.000$ p.u.. Consequently, V_{14} deviates from the previous equilibrium point, which fluctuates in the range of 0.97 - 1.04 p.u.. Based on Fig. 17(b), i_{14} significantly increases when $t\geq 2.45$ s. The major harmonic frequencies of the instantaneous current i_{14} are 17.5 Hz and 82.5 Hz (50 Hz ± 32.5 Hz), and the sub-synchronous current flows from the VSCs to the networks. As shown in Fig. 17(c), the SVC stimulates a linear LC resonance, whose combination of capacitance and network inductance matches the sub-synchronous frequency of the VSCs. Additionally, the current waveform of the SVC shows that the SVC functions as a harmonic amplifier.

TABLE III
PARAMETERS OF NETWORK AND VSC CONTROL FOR CASE STUDY SYSTEM

Parameter	Value
K_{Pid}, K_{Iid}, K_{Piq}, K_{Iiq} (SVG voltage control loop)	2.5 p.u., 1000 p.u., 2 p.u., 20 p.u.
V_{ref1}, V_{ref2}, V_{ref3} (reference of terminal voltage control)	1.005 p.u., 1.005 p.u., 1.005 p.u. ($t<2$ s) 1.005 p.u., 1.000 p.u., 1.005 p.u. ($t\geq 2$ s)
K_{Pi}, K_{Ii} (current control loop)	40 p.u., 6250 p.u.
X_{l1}, X_{l2}, X_{l3} (connection impedance)	0.0051 p.u., 0.0038 p.u., 0.0256 p.u.
$R_{6\text{-}10}$, $R_{8\text{-}11}$ (line resistance)	0.0017 p.u., 0.0054 p.u.
$X_{6\text{-}10}$, $X_{8\text{-}11}$ (line impedance)	0.0092 p.u., 0.0178 p.u.
X_{T1}, X_{T2}, X_{T3} (transformer impedance)	0.0586 p.u., 0.0586 p.u., 0.0576 p.u.

Calculated as (51), Table IV shows that the nonlinear index $\mu>\mu_p$ for the SVGs and $\mu\ll\mu_p$ for the SVC, which indicates that the SVGs are the main contributors to the nonlinearity. Hence, the nonlinearity is detected in the system. However, the hard limiting takes effect in only two SVGs. Therefore, the proposed method can only detect the nonlinear behavior in the system, but not its location. Furthermore, the precise localization method needs to be developed in future studies.

VII. CONCLUSION

This study proposes a method based on the HOS analysis for the hard-limiting DNB in the VSC control system in wind farms, wherein the PMSGs and VSGs are modeled using a unified VSC control model. The contributions are summarized as follows.

1) The effectiveness of the bi- and tri-spectra is proven when characterizing the nonlinear behavior induced by hard limiting in the VSC control system.

2) The effects of the linear parts in the VSC control system are eliminated using the bi- and tri-coherence, which facilitate the hard-limiting DNB with only the waveforms collecte at the terminal of the VSC. Additionally, the phase equation is proven to be a sufficient and unnecessary condition of the phase coupling phenomenon, which is not examined thoroughly in previous studies.

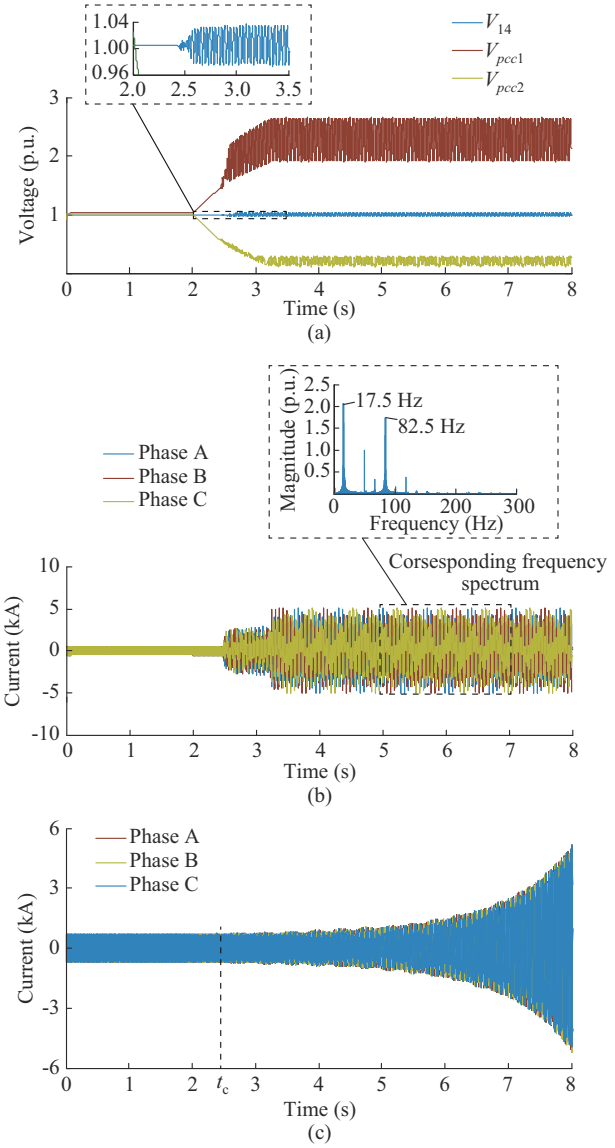

Fig. 17. Voltage and current waveforms. (a) Voltage amplitude. (b) Three-phase. (c) Three-phase currents of SVC.

TABLE IV
COMPARISON OF μ FOR HARMONIC SOURCE SEARCHING

Part	μ (p.u.)	Threshold μ_p (p.u.)
SVG_1	0.3727	0.1000
SVG_2	0.1598	
SVG_3	0.1043	
SVC	0.0079	

3) The detailed procedure is proposed to detect and classify the nonlinear behavior caused by the bi- or uni-lateral saturation hard limiting.

4) The data processing problems are solved in the DNB procedures based on the HOS, such as the "0/0" phenomenon and spectrum leakage, to improve the resolution and quality of the spectra.

Future studies include two aspects.

First, the HOS analysis is a measurement-based method. However, the extension of the proposed method to any equipment requires further examination. This study confirms the applicability of the HOS-based DNB to VSCs, which exist in energy storage equipment and flexible DC transmission systems, in addition to wind power systems as discussed in this study. Here, we do not investigate eliminating the effects of different parts of other devices (in the path from the hard limiter to the terminal).

Second, as discussed in Section VI-C, the DNB is not sufficient to constitute an effective control measure and generator tripping strategy when a self-sustained oscillation accident occurs. Therefore, a nonlinear oscillatory source localization method needs to be introduced.

APPENDIX A

TABLE AI
THE n^{th} COMPONENT OF BI-LATERAL SATURATION HARD LIMIT OUTPUT

n	A_n	B_n
0	0	0
1	0	$\dfrac{2a\sqrt{1-\frac{a^2}{A^2}}+2A\arcsin\frac{a}{A}}{\pi}$
2	0	0
3	0	$\dfrac{4a\left(1-\frac{a^2}{A^2}\right)^{3/2}}{3\pi}$
4	0	0
5	0	$\dfrac{4a\sqrt{1-\frac{a^2}{A^2}}\left(8a^4-11a^2A^2+3A^4\right)}{15A^4\pi}$
6	0	0
7	0	$\dfrac{48a\cos\left(7\arcsin\frac{a}{A}\right)+28A\sin\left(6\arcsin\frac{a}{A}\right)-21A\sin\left(8\arcsin\frac{a}{A}\right)}{84\pi}$

APPENDIX B

Based on the results in Section II-B, when self-sustained oscillation occurs, the output $y(t)$ of the bi-lateral saturation hard limiter contains the 3rd and 5th harmonics of the oscillation frequency with the same phase as that of the fundamental frequency. Without loss of generality, let its initial phase be zero, that is,

$$y(t)=B_1\sin(2\pi ft)+B_3\sin(2\pi\times 3ft)+B_5\sin(2\pi\times 5ft) \tag{B1}$$

where B_1, B_3, and B_5 are the Fourier coefficients of the 1st, 3rd, and 5th Fourier harmonics, respectively.

The Fourier transform is performed three times on the third-order autocorrelation function of $y(t)$. Thus, the tri-spectrum of $y(t)$ can be derived as:

$$\begin{cases} R_f(\tau_1,\tau_2,\tau_3)=f\int_0^{1/f}y(t)\,y(t+\tau_1)\,y(t+\tau_2)\,y(t+\tau_3)\,\mathrm{d}t \\ T_y(\omega_1,\omega_2,\omega_3)=\int_{-\infty}^{\infty}\int_{-\infty}^{\infty}\int_{-\infty}^{\infty}R_f(\tau_1,\tau_2,\tau_3)\,\mathrm{e}^{-\mathrm{j}2\pi(\omega_1+\omega_2+\omega_3)}\mathrm{d}\tau_1\,\mathrm{d}\tau_2\,\mathrm{d}\tau_3 \end{cases} \tag{B2}$$

TABLE AII
THE n^{th} COMPONENT OF UNI-LATERAL SATURATION HARD LIMIT OUTPUT

n	A_n	B_n
0	$a+2A_0-\frac{2}{\pi}\sqrt{1-\frac{a^2}{A^2}}A-\frac{2\mathrm{a}}{\pi}\arcsin\frac{a}{A}$	$a+2A_0-\frac{2}{\pi}\sqrt{1-\frac{a^2}{A^2}}A-\frac{2\mathrm{a}}{\pi}\arcsin\frac{a}{A}$
1	0	$\frac{2a\sqrt{1-\frac{a^2}{A^2}}+A\pi+2A\arcsin\frac{a}{A}}{2\pi}$
2	$\frac{2\sqrt{1-\frac{a^2}{A^2}}\left(-a^2+A^2\right)}{3A\pi}$	0
3	0	$\frac{2a\left(1-\frac{a^2}{A^2}\right)^{3/2}}{3\pi}$
4	$\frac{2\sqrt{1-\frac{a^2}{A^2}}\left(6a^4-7a^2A^2+A^4\right)}{15A^3\pi}$	0
5	0	$\frac{2a\left(3+\frac{8a^4}{A^4}-\frac{11a^2}{A^2}\right)\sqrt{1-\frac{a^2}{A^2}}}{15\pi}$
6	$\frac{2\sqrt{1-\frac{a^2}{A^2}}}{105A^5\pi}\left(-80a^6+128a^4A^2-51a^2A^4+3A^6\right)$	0
7	0	$\frac{1}{168\pi}\left(48\mathrm{a}\cos\left(7\arcsin\frac{a}{A}\right)+28\mathrm{A}\sin\left(6\arcsin\frac{a}{A}\right)-21\mathrm{A}\sin\left(8\arcsin\frac{a}{A}\right)\right)$

Additionally, the tri-spectrum has 96 symmetrical regions [35]. Therefore, a symmetrical region in the result of $T_y(\omega_1,\omega_2,\omega_3)$ can be used for analysis to completely describe the entire trispectrum. Considering $\left\{(\omega_1,\omega_2,\omega_3)\middle|0\le\omega_1\le\omega_2\le\omega_3\right\}$, $T_y(\omega_1,\omega_2,\omega_3)$ is calculated as:

$$T_y(\omega_1,\omega_2,\omega_3)=\frac{B_1^3B_3\pi^{3/2}}{4\sqrt{2}}\delta(\omega_1-2\pi f)\delta(\omega_2-2\pi f)\delta(\omega_3-2\pi f)+\frac{B_1^2B_3B_5\pi^{3/2}}{4\sqrt{2}}\delta(\omega_1-2\pi f)\delta(\omega_2-2\pi f)\delta(\omega_3-6\pi f) \tag{B3}$$

$T_y(\omega_1,\omega_2,\omega_3)$ is a finite maximum if and only if $\omega_1=\omega_2=\omega_3=2\pi f$ or $\omega_1=\omega_2=2\pi f,\omega_3=6\pi f$; otherwise, it is zero. Therefore, two peaks can be observed at the *x*-*y*-*z* coordinates $(2\pi f,2\pi f,2\pi f)$ and $(2\pi f,2\pi f,6\pi f)$ in the four-dimensional (4D) graph of $\left\{(\omega_1,\omega_2,\omega_3,T_y(\omega_1,\omega_2,\omega_3))\middle|0\le\omega_1\le\omega_2\le\omega_3\right\}$. For an easy intuitive visualization of the graphs, when the area is extended to $\left\{(\omega_1,\omega_2,\omega_3)\middle|\omega_1\ge0,\omega_2\ge0,\omega_3\ge0\right\}$, four peaks at $(2\pi f,2\pi f,2\pi f)$, $(2\pi f,2\pi f,6\pi f)$, $(2\pi f,6\pi f,2\pi f)$, and $(6\pi f,2\pi f,2\pi f)$ occur.

The power spectrum of $y(t)$ is expressed as:

$$P_y(\omega)=\int_{-\infty}^{\infty}f\int_0^{1/f}y(t)\,y(t+\tau)\,\mathrm{d}t\cdot\mathrm{e}^{-\mathrm{j}2\pi\omega}\mathrm{d}\tau=\frac{1}{2}B_1^2\sqrt{\frac{\pi}{2}}\delta(\omega-2\pi f)+\frac{1}{2}B_3^2\sqrt{\frac{\pi}{2}}\delta(\omega-6\pi f)+\frac{1}{2}B_5^2\sqrt{\frac{\pi}{2}}\delta(\omega-10\pi f) \tag{B4}$$

According to (B3) and (B4), the tri-coherence spectrum $\left(\left\{(\omega_1,\omega_2,\omega_3)\middle|\omega_1\ge0,\omega_2\ge0,\omega_3\ge0\right\}\right)$ can be expressed as:

$$tric_y(\omega_1,\omega_2,\omega_3)=\frac{\left|T_y(\omega_1,\omega_2,\omega_3)\right|}{\sqrt{P_y(\omega_1+\omega_2+\omega_3)P_y(\omega_1)P_y(\omega_2)P_y(\omega_3)}} \tag{B5}$$

In (B5), the tri-coherence spectrum of $y(t)$ reaches its peak if and only if $\{\omega_1,\omega_2,\omega_3\}=\{2\pi f,2\pi f,2\pi f\}$, $\{2\pi f,2\pi f,6\pi f\}$, $\{2\pi f,6\pi f,2\pi f\}$, or $\{6\pi f,2\pi f,2\pi f\}$.

When $\{\omega_1,\omega_2,\omega_3\}=\{2\pi f,2\pi f,2\pi f\}$, (B5) is calculated as (B6). When $\{\omega_1,\omega_2,\omega_3\}=\{2\pi f,2\pi f,6\pi f\}$, $\{2\pi f,6\pi f,2\pi f\}$, or $\{6\pi f,2\pi f,2\pi f\}$, (B5) is calculated as (B7).

$$tric_y(2\pi f,2\pi f,2\pi f)=\frac{\frac{B_1^3B_3\pi^{3/2}}{4\sqrt{2}}\frac{1}{\sqrt{2\pi}}\frac{1}{\sqrt{2\pi}}\frac{1}{\sqrt{2\pi}}}{\sqrt{\frac{1}{2}B_3^2\sqrt{\frac{\pi}{2}}\frac{1}{\sqrt{2\pi}}\frac{1}{2}B_1^2\frac{1}{\sqrt{2\pi}}\sqrt{\frac{\pi}{2}}\frac{1}{2}B_1^2\frac{1}{\sqrt{2\pi}}\sqrt{\frac{\pi}{2}}\frac{1}{2}B_1^2\frac{1}{\sqrt{2\pi}}\sqrt{\frac{\pi}{2}}}}=1 \tag{B6}$$

$$tric_y(2\pi f,2\pi f,6\pi f)=\frac{\frac{B_1^2B_3B_5\pi^{3/2}}{4\sqrt{2}}\frac{1}{\sqrt{2\pi}}\frac{1}{\sqrt{2\pi}}\frac{1}{\sqrt{2\pi}}}{\sqrt{\frac{1}{2}B_5^2\sqrt{\frac{\pi}{2}}\frac{1}{\sqrt{2\pi}}\frac{1}{2}B_3^2\frac{1}{\sqrt{2\pi}}\sqrt{\frac{\pi}{2}}\frac{1}{2}B_1^2\frac{1}{\sqrt{2\pi}}\sqrt{\frac{\pi}{2}}\frac{1}{2}B_1^2\frac{1}{\sqrt{2\pi}}\sqrt{\frac{\pi}{2}}}}=1 \tag{B7}$$

In (B5), $tric_y(\omega_1,\omega_2,\omega_3)\ge0$. Therefore, the range of the corresponding tri-coherence value of each *x*-*y*-*z* coordinate in the tri-coherence spectrum is $[0,1]$. The larger the tri-coherence value, the stronger the nonlinear phase coupling among the three frequencies corresponding to the coordinate (the stronger the nonlinearity).

In (B1), when $y(t)$ extends to $y(t)=\sum_{n=0}^{+\infty}B_{2n+1}\sin(2\pi(2n+1ft)$, according to (9), which accurately represents the output of the bi-lateral saturation hard limiter, it can be proved that in the

4D graph of $\left\{\left(\omega_1,\omega_2,\omega_3,tric_y\left(\omega_1,\omega_2,\omega_3\right)\right)\middle|\omega_1\geq 0,\omega_2\geq 0,\omega_3\geq 0\right\}$, peaks exist at the *x*-*y*-*z* coordinates $\left((2i+1)\cdot 2\pi f,(2j+1)\cdot 2\pi f,(2k+1)\cdot 2\pi f\right)(i,j,k=0,1,2,\ldots)$.

REFERENCES

[1] S. Zhang, J. Wei, X. Chen *et al*., "China in global wind power development: role, status and impact," *Renewable and Sustainable Energy Reviews*, vol. 127, p. 109881, Jul. 2020.

[2] J. Shair, X. Xie, L. Wang *et al*., "Overview of emerging subsynchronous oscillations in practical wind power systems," *Renewable and Sustainable Energy Reviews*, vol. 99, pp. 159-168, Jan. 2019.

[3] E. Ebrahimzadeh, F. Blaabjerg, X. Wang *et al.*, "Modeling and identification of harmonic instability problems in wind farms," in *Proceedings of the 8th Annual IEEE Energy Conversion Congress & Exposition (ECCE)*, Milwaukee, Wisconsin, USA, Sept. 2016, pp. 1-6.

[4] A. Shafiu, O. Anaya-Lara, G. Bathurst *et al.*, "Aggregated wind turbine models for power system dynamic studies," *Wind Engineering*, vol. 30, no. 3, pp. 171-185, May 2006.

[5] J. Bi, W. Du, and H. F. Wang, "An aggregation method of wind farms model for studying power system low frequency power oscillation," in proceedings of *2017 2nd International Conference on Power and Renewable Energy (ICPRE)*, Chengdu, China, Sept. 2017, pp. 422-427.

[6] J. Sun, "Impedance-based stability criterion for grid-connected inverters," *IEEE Transactions on Power Electronics*, vol. 26, no. 11, pp. 3075-3078, Apr. 2011.

[7] L. Fan and Z. Miao, "Nyquist-stability-criterion-based SSR explanation for Type-3 wind generators," *IEEE Transactions on Energy Conversion*, vol. 27, no. 3, pp. 807-809, May 2012.

[8] F. Zhao, L. Wu, J. Zhang *et al.*, "Suppression method of parallel-damping controller for DFIG," *Journal of Engineering*, vol. 2017, no. 13, pp. 880-884, Oct. 2017.

[9] L. Sainz, M. Cheah-Mane, L. Monjo *et al.*, "Positive-net-damping stability criterion in grid-connected VSC systems," *IEEE Journal of Emerging & Selected Topics in Power Electronics*, vol. 5, no. 4, pp. 1499-1512, May 2017.

[10] X. Xie, H. Liu, J. He *et al.*, "On new oscillation issues of power systems," *Proceedings of the CSEE*, vol. 38, no. 10, pp. 2821-2828, May 2018.

[11] S. Shah, P. Koralewicz, V. Gevorgian *et al.*, "Large-signal impedance-based modeling and mitigation of resonance of converter-grid systems," *IEEE Transactions on Sustainable Energy*, vol. 10, no. 3, pp. 1439-1449, Jul. 2019.

[12] Y. Xu, Z. Gu, and K. Sun, "Characterization of subsynchronous oscillation with wind farms using describing function and generalized Nyquist criterion," *IEEE Transactions on Power Systems*, vol. 35, no. 4, pp. 2783-2793, Jul. 2020.

[13] T. Wu, Q. Jiang, J. Shair *et al.*, "Inclusion of current limiter nonlinearity in the characteristic analysis of sustained subsynchronous oscillations in grid-connected PMSGs," *IEEE Transactions on Energy Conversion*, vol. 36, no. 3, pp. 2416-2426, Sep. 2021.

[14] A. Xue, Y. Wang, X. Fu *et al.*, "Analysis of switched subsynchronous oscillation and its non-smooth bifurcation characteristics in doubly-fed system with SVG," *Power System Technology*, vol. 45, no. 3, pp. 918-926, Mar. 2021.

[15] G. Xing, Y. Min, L. Chen *et al.*, "Limit induced bifurcation of grid-connected VSC caused by current limit," *IEEE Transactions on Power Systems*, vol. 36, no. 3, pp. 2717-2720, May 2021.

[16] A. Swami and J. M. Mendel, "Cumulant-based approach to the harmonic retrieval problem," in *Proceedings of 1988 International Conference on Acoustics, Speech, and Signal Processing (ICASSP 88),* New York, USA, Apr. 1988, pp. 2264-2265.

[17] K. Lii and M. Rosenblatt, "Deconvolution and estimation of transfer function phase and coefficients for nonGaussian linear processes," *The Annals of Statistics*, vol. 10, no. 4, pp. 1195-1208, Dec. 1982.

[18] G. Zhang, T. Shi, and S. Yang, "A method for extracting mechanical faults features based on higher-order statistics," *Journal of Huazhong University of Science and Technology*, vol. 27, no. 3, pp. 6-8, Mar. 1999.

[19] M. Rosenblatt and J. W. V. Ness, "Estimation of the bispectrum," *The Annals of Mathematical Statistics*, vol. 36, no. 4, pp. 1120-1136, Aug. 1965.

[20] D. R. Brillinger, "An introduction to polyspectra," *The Annals of Mathematical Statistics*, vol. 36, no. 5, pp. 1351-1374, Oct. 1965.

[21] A. M. Tekalp and A. T. Erdem, "Higher-order spectrum factorization in one and two dimensions with applications in signal modeling and nonminimum phase system identification," *IEEE Transactions on Acoustics Speech & Signal Processing*, vol. 37, no. 10, pp. 1537-1549, Oct. 1989.

[22] T. W. S. Chow and G. Fei, "Three phase induction machines asymmetrical faults identification using bispectrum," *IEEE Transactions on Energy Conversion*, vol. 10, no. 4, pp. 688-693, Dec. 1995.

[23] B. Jang, C. Shin, E. J. Powers *et al.*, "Machine fault detection using bicoherence spectra," in *Proceedings of the 21st IEEE Instrumentation and Measurement Technology Conference*, Como, Italy, May 2004, pp. 1661-1666.

[24] Y. Jiang, C. Tang, X. Zhang *et al.*, "A novel rolling bearing defect detection method based on bispectrum analysis and cloud model-improved EEMD," *IEEE Access*, vol. 8, pp. 24323-24333, Jan. 2020.

[25] X. Chen, W. Xu, Y. Liu *et al.*, "Bearing corrosion failure diagnosis of doubly fed induction generator in wind turbines based on stator current analysis," *IEEE Transactions on Industrial Electronics*, vol. 67, no. 5, pp. 3419-3430, May 2020.

[26] J. R. Stack, R. G. Harley, and T. G. Habetler, "An amplitude modulation detector for fault diagnosis in rolling element bearings," *IEEE Transactions on Industrial Electronics*, vol. 51, no. 5, pp. 1097-1102, Oct. 2004.

[27] Y. Li, Z. Han, and Z. Wang, "Research on a signal separation method based on Vold-Kalman filter of improved adaptive instantaneous frequency estimation," *IEEE Access*, vol. 8, pp. 112170-112189, Jun. 2020.

[28] J. H. Taylor, *Describing Functions*. Hoboken: Wiley Encyclopedia of Electrical and Electronics Engineering, 2001.

[29] Z. An, C. Shen, Z. Zheng *et al.*, "Assessment method for equivalent models of wind farms based on direct-driven wind generators considering randomness," *Proceedings of the CSEE*, vol. 38, no. 22, pp. 6511-6519, Nov. 2018.

[30] K. M. Alawasa, Y. A. R. I. Mohamed, and W. Xu, "Active mitigation of subsynchronous interactions between PWM voltage-source converters and power networks," *IEEE Transactions on Power Electronics*, vol. 29, no. 1, pp. 121-134, Mar. 2013.

[31] K. M. Alawasa, Y. A. R. I. Mohamed, and W. Xu, "Modeling, analysis, and suppression of the impact of full-scale wind-power converters on subsynchronous damping," *IEEE Systems Journal*, vol. 7, no. 4, pp. 700-712, Jan. 2013.

[32] W. Song and A. Q. Huang, "Fault-tolerant design and control strategy for cascaded H-bridge multilevel converter-based STATCOM," *IEEE Transactions on Industrial Electronics*, vol. 57, no. 8, pp. 2700-2708, Aug. 2010.

[33] X. Hou, Y. Sun, H. Han *et al*., "A general decentralized control scheme for medium-/high-voltage cascaded STATCOM," *IEEE Transactions on Power Systems*, vol. 33, no. 6, pp. 7296-7300, Nov. 2018.

[34] C. L. Nikias and M. R. Raghuveer, "Bispectrum estimation: a digital signal processing framework," *Proceedings of the IEEE*, vol. 75, no. 7, pp. 869-891, Jul. 1987.

[35] L. A. Pflug, G. E. Ioup, J. W. Ioup *et al*., "Properties of higher-order correlations and spectra for bandlimited, deterministic transients," *The Journal of the Acoustical Society of America*, vol. 91, no. 2, pp. 975-988, Feb. 1992.

[36] P. A. M. Dirac, "The quantum theory of the emission and absorption of radiation," *Proceedings of the Royal Society of London*, vol. 114, no. 767, pp. 243-265, Mar. 1927.

[37] M. A. A. S. Choudhury, S. L. Shah, and N. F. Thornhill, "Diagnosis of poor control-loop performance using higher-order statistics," *Automatica*, vol. 40, no. 10, pp. 1719-1728, Oct. 2004.

[38] *Quality of Electric Energy Supply – Harmonics in Public Supply Network*, Chinese National Standard 14549-1993.

[39] K. L. Siu, J. M. Ahn, K. Ju *et al.*, "Statistical approach to quantify the presence of phase coupling using the bispectrum," *IEEE Transactions on Biomedical Engineering*, vol. 55, no. 5, pp. 1512-1520, Apr. 2008.

[40] Z. Yanbing, L. Yibing, A. Hongwen *et al.*, "Fault recognition of large steam turbine based on higher order spectral features of vibration signals," in *Proceedings of 2011 IEEE International Conference on Mechatronics and Automation*, Beijing, China, Aug. 2011, pp. 1572-1577.

[41] C. Qiu, Z. Xue, and P. Shao, "An identification method for weak motor fault eigenfrequencies based on multitaper bispectrum," in *Proceedings of 2010 International Conference on Intelligent Control and Information Processing*, Dalian, China, Aug. 2010, pp. 236-239.

Zetian Zheng received the B.E. degree from Tsinghua University, Beijing,

China, in 2017, in electrical engineering. From 2017, he has been a Ph.D. student with the Department of Electrical Engineering, Tsinghua University. His research interests include power system stability and control.

Shaowei Huang received the B.E. and Ph.D. degrees from the Department of Electrical Engineering, Tsinghua University, Beijing, China, in 2006 and 2011, respectively. From 2011 to 2013, he held a postdoctoral position at the Department of Electrical Engineering, Tsinghua University, where he is currently an Associate Professor. His research interests include power system modeling and simulation, power system parallel and distributed computing, complex systems and its application in power systems, and artificial intelligence.

Qiangsheng Bu received the B. E. degree in electrical engineering from Southeast University, Nanjing, China, in 2006, and the M.Sc. degree electrical engineering from Southeast University, in 2009. He is currently working as a Senior Engineer in State Grid Jiangsu Electric Power Co., Ltd. Research Institute, Nanjing, China. His research interests include power system automation, relay protection, control and protection of distributed new energy.

Chen Shen received the B.E. and Ph.D. degrees in electrical engineering from Tsinghua University, Beijing, China, in 1993 and 1998, respectively. From 1998 to 2001, he was a Postdoc Research Fellow with the Department of Electrical Engineering and Computer Science, University of Missouri Rolla, Rolla, USA. From 2001 to 2002, he was a Senior Application Developer with ISO New England, Inc., Holyoke, USA. Since 2009, he has been a Professor with the Department of Electrical Engineering, Tsinghua University. He is currently the Director of the Energy Digitization Research Center, Sichuan Energy Internet Research Institute, Tsinghua University. His research interests include power system analysis and control, renewable energy generation, and smart grids.

Jun Yan received the B.E. degree in automation engineering and the M.E. degree in electrical engineering from Lanzhou University of Technology, Lanzhou, China, in 2007 and 2011, respectively. He received the Ph.D. degree in electrical engineering from the Army Engineering University of PLA, Nanjing, China, in 2018. He worked as a Postdoctor in the Department of Electrical Engineering, Tsinghua University, from 2019 to 2021. He is currently working as a Lecturer in Army Engineering University, Nanjing, China. His research interests include power system dynamics, input-state stability, the energy-structure theory and its application to the oscillation locating.